



Article

<https://doi.org/10.1038/s41558-024-02171-3>

Emergence of a climate oscillation in the Arctic Ocean due to global warming

Received: 16 April 2023

Accepted: 24 September 2024

Published online: 11 November 2024

Check for updates

Soong-Ki Kim¹ & Soon-Il An^{1,2,3}

Global warming is expected to be able to trigger abrupt transitions in various components of the climate system. Most studies focus on abrupt changes in the mean state of the system, while transitions in climate variability are less well understood. Here, we use multimodel simulations to show that sea-ice loss in the Arctic can trigger a critical transition in internal variability that leads to the emergence of a new climate oscillation in the Arctic Ocean. The intensified air–sea interaction due to sea-ice melt causes an oscillatory behaviour of surface temperatures on a multidecadal timescale. Our results suggest that a new mode of internal variability will emerge in the Arctic Ocean when sea ice declines below a critical threshold.

Future projections from the latest generation of global climate models show that the Arctic will experience dramatic changes due to global warming^{1,2}. Arctic sea-ice cover is projected to rapidly decrease and become practically ice-free in summer within the twenty-first century under all levels of anthropogenic emissions scenarios^{3,4}. This massive sea-ice loss would expand the area of open ocean and intensify the interaction between the atmosphere and the ocean over the Arctic.

As demonstrated by the cases of El Niño/Southern Oscillation⁵, Indian Ocean Dipole⁶ and Atlantic Multidecadal Oscillation⁷, air–sea interaction processes and associated coupled feedbacks are some of the key ingredients for climate oscillation. Large-scale air–sea interaction processes give rise to a mode of climate oscillation, a recurring cycle of climate variables that deviate from the background climate noise. Notably, ref. 5 demonstrated that El Niño/Southern Oscillation theoretically ceases to occur if the air–sea interaction process is sufficiently weakened. This suggests that climate oscillation mode can be switched on or off following changes in background climatological state. Therefore, the Arctic sea-ice melt due to global warming may activate a new climate oscillation in the Arctic Ocean that does not currently manifest in the present sea-ice-covered state. Although atmospheric scale variabilities in the Arctic have been previously well recognized^{8–17}, the hypothetical air–sea coupled mode, which is expected to emerge in a warm climate, has not yet been systematically explored in current literature.

In this Article, we show multiple lines of evidence that a climate oscillation characterized by a multidecadal variation in annual surface temperature can emerge in the Arctic due to global warming. We use a

total of 134 simulations run from three climate model intercomparison project archives—the Climate Model Intercomparison Project Phase 6 (CMIP6)^{18,19}, Long Run Model Intercomparison Project (LongRunMIP)²⁰ and Pliocene Model Intercomparison Project Phase 2 (PlioMIP2)^{21–23}. Our analysis will focus mainly on the annual mean surface temperature anomaly over the central Arctic Ocean (80° N–90° N) (the domain does not include the marginal Arctic seas such as the Barents Sea and Greenland Sea).

Evidence from the CMIP6 archive

We begin the analysis of annual surface temperature variability in the projected warm climate using the historical and Shared Socioeconomic Pathway 5–8.5 (SSP5–8.5) experiment output from the CMIP6 archive. The SSP5–8.5 is the high greenhouse gas emissions scenario for forcing fossil-fuelled development with a radiative forcing level of 8.5 W m⁻² in 2100. We use merged historical and SSP5–8.5 runs spanning 1850 to 2099 for 41 models (Supplementary Table 1 and Methods). The multimodel ensemble mean shows a 5 °C increase in global mean surface temperature (GMST) and 95% decrease in summer Arctic sea-ice area from 1850 to 2099 (Fig. 1a,c). Thus, the CMIP6 ensemble here shows the response of Arctic surface temperature variability in a warm climate where sea ice is mostly diminished (Fig. 1d). We perform a spectral analysis on the annual mean surface temperature anomaly of each ensemble member (Methods).

The CMIP6 analysis provides ensemble-wise evidence for the emergence of a multidecadal oscillation in the projected warm climate in the twenty-first century. The spectral analysis shows that the

¹Irreversible Climate Change Research Center, Yonsei University, Seoul, Republic of Korea. ²Department of Atmospheric Sciences, Yonsei University, Seoul, Republic of Korea. ³Division of Environmental Science and Engineering, Pohang University of Science and Technology (POSTECH), Pohang, Republic of Korea. e-mail: sian@yonsei.ac.kr

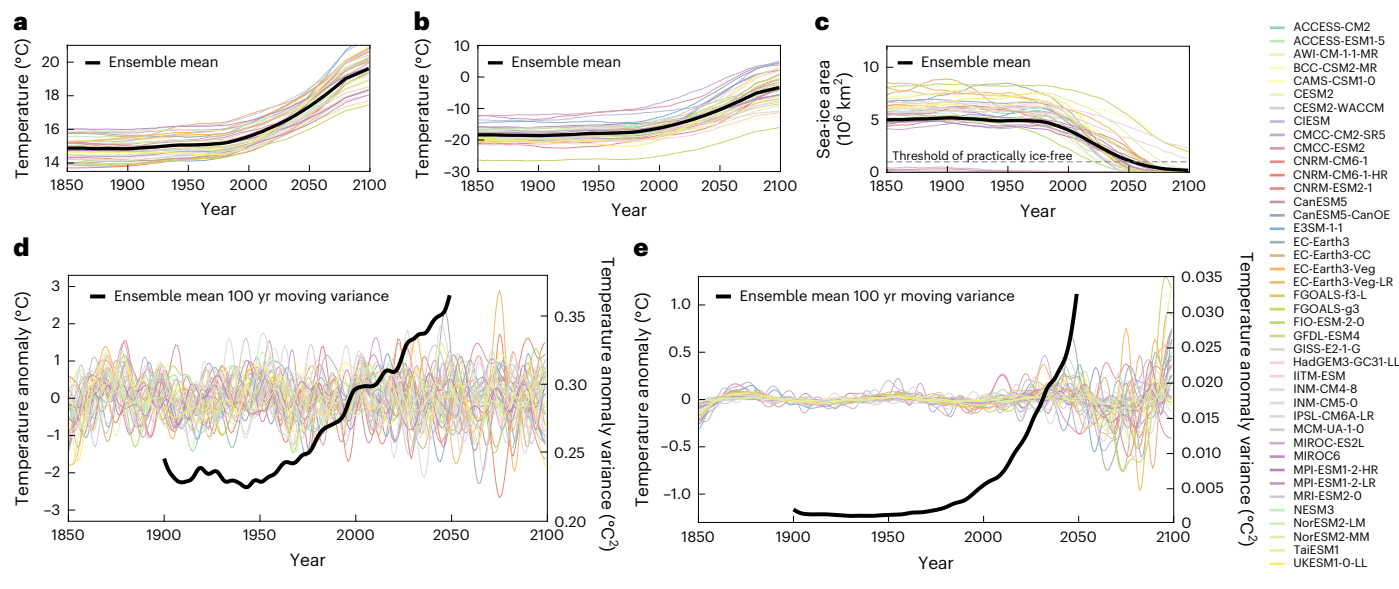


Fig. 1 | Changes in the Arctic temperature for 1850–2099 in the CMIP6 historical and SSP5–8.5 experiment. **a–c**, Changes in global and Arctic climate. **a**, GMST. **b**, Arctic surface temperature. **c**, September Arctic sea-ice area. The dashed grey line is the threshold of a practically ice-free state (sea-ice area less than 10^6 km^2). All three variables are 40-year moving means, which show their long-term trend. The black thick line is a multimodel ensemble mean. **d**, Changes in the Arctic surface temperature anomaly. The anomaly is defined as

a deviation from the quadratic trend of Arctic surface temperature for 1850–2099 (Methods). Left axis: time series of Arctic surface temperature anomaly (coloured lines). A 10-year low-pass filter is applied to display multidecadal variability. Right axis: multimodel ensemble mean of the 100-year moving variance of Arctic surface temperature anomaly (black line). **e**, Same as **d**, but for the Arctic Ocean temperature anomaly at 5 m depth.

multidecadal surface temperature variability is significantly intensified in the twenty-first century (Fig. 2a). The ensemble mean spectral peak of the surface temperature variability over 1850–1944 is below the climate noise level, indicating that the variability is probably driven by stochastic weather forcing. By contrast, in 2000–2099, the spectral peak intensifies and becomes equal to or significantly above the climate noise level, indicating that the variability is likely to be ‘oscillation’ caused by low-frequency dynamics, which is clearly distinct from stochastic variability.

To resolve the time evolution of the spectra in detail, we perform a wavelet analysis. The ensemble mean wavelet power spectrum shows that a 10–20-year surface temperature variability significantly strengthens in 2020 (Fig. 2b and Supplementary Fig. 1). This emerging strong narrow-band 10–20-year variability persists after 2020 (ensemble mean GMST 15.8 °C), shows a local peak in 2030 (ensemble mean GMST 16.5 °C) and further intensifies beyond 2060 (ensemble mean GMST 18.0 °C). The peak spectral period of this emerging variability slightly increases from 14 to 18 years with increasing GMST.

The changes in surface temperature variability occur with the increase of the air–sea coupling strength (Extended Data Fig. 1 and Fig. 1d,e) by the increase in open ocean area from sea-ice loss. Therefore, the increasing coupling strength possibly triggers the transition of surface temperature variability to a ‘quasi-periodic oscillation’, which is likely to be driven by coupled air–sea dynamics. Since the ocean is a slow-response component, the increasing air–sea coupling would increase the memory of the atmosphere, leading to an increase in the period and amplitude of the surface temperature oscillation. This consistently explains the change in the wavelet spectra in 2020–2099 (Fig. 2b).

Evidence from the LongRunMIP archive

In the CMIP6 ensemble, the oscillation lasts less than 100 years. This time frame is not long enough to reliably detect and analyse the multidecadal oscillation signal, which has a spectral period of 10–50 years. To investigate the oscillation in detail, we analyse the simulations from the LongRunMIP archive. The LongRunMIP provides a fully coupled

climate model simulation longer than 1,000 years over a wide range of high CO₂ levels. The typical forcing scenario of LongRunMIP is an instantaneous doubling (abrupt2x), quadrupling (abrupt4x) and octupling (abrupt8x) of atmospheric CO₂ level. After the abrupt increase in CO₂, the forcing is stabilized for typically longer than 1,000 years. Thus, it offers a unique opportunity to study the internal climate oscillation across a wide array of quasi-equilibrated warm climate. Our LongRunMIP analysis sample includes a total of 39 simulations from 13 models (Supplementary Table 2). We specifically use the last 1,000 years of the simulations where the GMST sufficiently reaches a quasi-equilibrium state (some models are selected for less than 1,000 years because of the short duration, but all of them are longer than 500 years). The LongRunMIP ensemble offers an array of climate simulations under the GMST range of 12.8 °C to 28.6 °C. We perform the multitaper power spectrum analysis on the annual mean Arctic surface temperature anomaly for each ensemble member (Extended Data Fig. 2) and compile the results by their GMST level (Methods).

The LongRunMIP ensemble members show pronounced changes in the multitaper spectrum of the Arctic surface temperature anomaly with increasing GMST level. The multitaper spectrum composite of the LongRunMIP ensemble shows an intensification of spectral power over a period of 10–50 years as the GMST increases (Fig. 3a). The spectrum composite for the GMST range of 12 °C to 15 °C shows a weak multidecadal spectrum signal without a clear spectral peak. By contrast, the spectrum composite group of GMST larger than 18 °C, in which all ensemble members exhibit a practical summer ice-free state (sea-ice area less than 10^6 km^2), shows a clear and strong multidecadal spectral peak, significantly above the climate noise level. In particular, the spectral composite group of GMST greater than 24 °C shows strong spectral peaks at 18, 22 and 37 years. These results indicate that the LongRunMIP ensemble provides clear evidence for the emergence of the multidecadal oscillation in a warm climate where the sea ice is mostly diminished, as previously shown using the CMIP6 ensemble.

Note that the forcing scenario of LongRunMIP is different from that of the CMIP6 simulation. LongRunMIP is a simulation of equilibrium warming, while CMIP6 is a transient warming simulation.

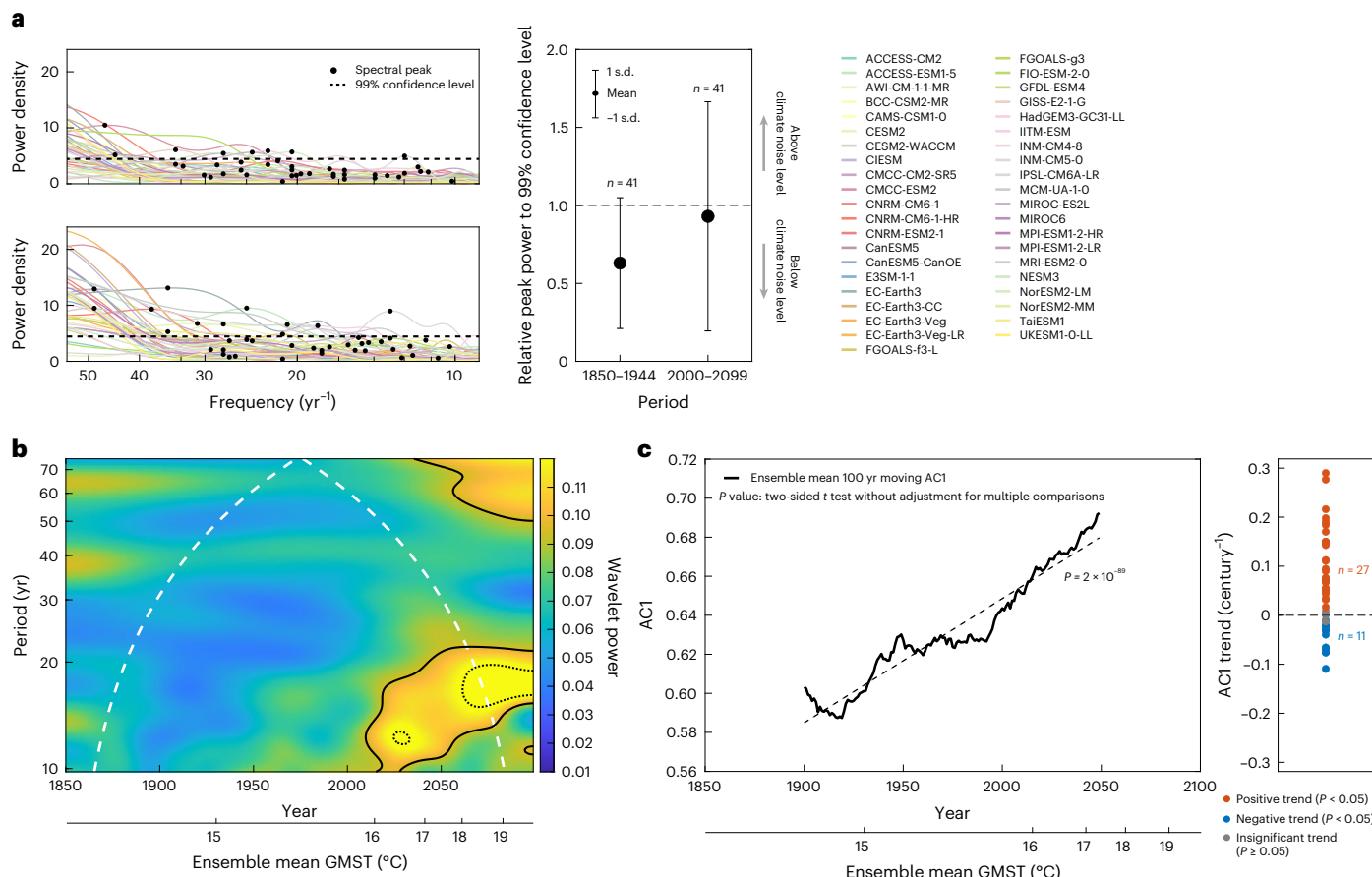


Fig. 2 | Changes in the Arctic surface temperature anomaly for 1850–2099 in the CMIP6 historical and SSP5–8.5 experiment. The anomaly is defined as a deviation from the quadratic trend of Arctic surface temperature for 1850–2099 (Methods). **a**, The power spectrum of Arctic surface temperature anomaly for 1850–1949 (left upper panel) and 2000–2099 (left lower panel). The black dashed line represents the 99% confidence level for red noise. The spectral peak (maximum local peak) is marked with the black dot. Right panel: the multimodel statistics of the spectral peak for 1850–1949 and 2000–2099; the relative spectral peak to the 99% confidence level. The black dot is the multimodel ensemble mean; the error bar represents the mean ± 1 s.d. range. **b**, The multimodel ensemble mean wavelet power spectrum of the Arctic surface temperature anomaly. The wavelet power spectrum is calculated for each model, and then the average is taken. The Morse wavelet is used. The lower horizontal axis displays the corresponding

multimodel ensemble mean GMST to year (black thick line in Fig. 1a). The cone of influence of the wavelet is represented by the white dashed line. Mean $+ 1$ s.d. and mean $+ 2$ s.d. of piControl wavelet power are shown as the black thick line and black dashed line, respectively (see Methods for details). The wavelet power spectrum using Morlet wavelet is shown in Supplementary Fig. 1. **c**, The multimodel ensemble mean 100-year moving AC1 of Arctic surface temperature anomaly (left panel); the linear trend of AC1 (dashed line). The lower horizontal axis displays the corresponding multimodel ensemble mean GMST to year (black thick line in Fig. 1a). Right panel: the linear trend of 100-year moving AC1 for each model. Models with a significant positive trend ($P < 0.05$) are marked with an orange dot, those with a significant negative trend ($P < 0.05$) are marked with a blue dot, and models with an insignificant trend ($P \geq 0.05$) are marked with a grey dot. Note that an unfiltered temperature time series is used for the results in **a–c**.

Nevertheless, the analysis of these two types of simulations shows that the oscillation emerges consistently in both transient and equilibrium warm climates, consistent with our oscillation emergence hypothesis.

Detailed characteristics and dynamics of the oscillation

Next, we investigate the detailed characteristics of the oscillation using the Community Earth System Model (CESM) 1.0.4 experiments from the LongRunMIP ensemble, which show pronounced changes in the surface temperature variability in a warm climate. We first look at an entire array of CESM 1.0.4 experiments (Extended Data Fig. 3a,b). As marked by the pronounced intensification of the multidecadal spectral signal (Extended Data Fig. 3c,d), the oscillation emerges in the abrupt4x and abrupt8x, where GMST rises to more than 20.0°C and summer sea ice becomes a practically ice-free state. The air-sea coupling strength, indicated by the correlation between surface air temperature and ocean temperature anomaly with depth, considerably increases in the abrupt4x and abrupt8x relative to the control and abrupt2x (Extended Data Fig. 3e). This shows that the oscillation

emerges when the air-sea coupling is strengthened due to the decrease in sea-ice area.

To understand the dynamical mechanism of the oscillation, we analyse the CESM1.0.4 abrupt4x experiment in detail. Ekman transport, a wind-driven ocean current, can occur actively in the ocean where sea ice is mostly diminished. The Ekman advection budget analysis (Methods and Supplementary Discussion 1) shows that the temperature advection by anomalous vertical Ekman transport explains 66% of the total tendency of the surface temperature anomaly (Extended Data Fig. 4a) and has a nearly in-phase relationship with it (Extended Data Fig. 4b). This indicates that anomalous vertical Ekman transport, which is driven mainly by the wind stress curl, is the primary driver for the surface temperature changes. The wind stress curl shows a nearly in-phase relationship with the temperature tendency (Extended Data Fig. 5a) and induces the positive temperature change with a lag of 10 years (Extended Data Fig. 5b). These results are physically interpreted as follows: a positive (negative) wind stress curl causes Ekman upwelling (downwelling) and results in warm (cold) advection and increases (decreases) the surface temperature.

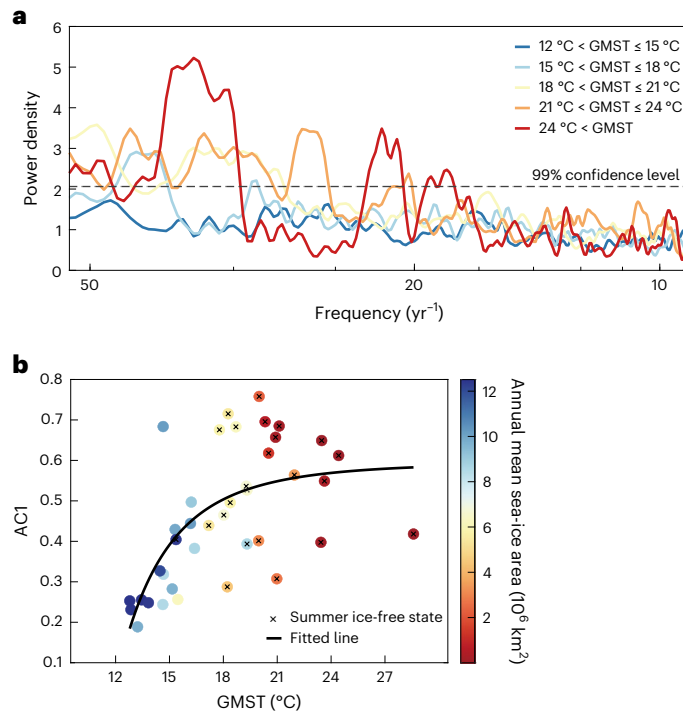
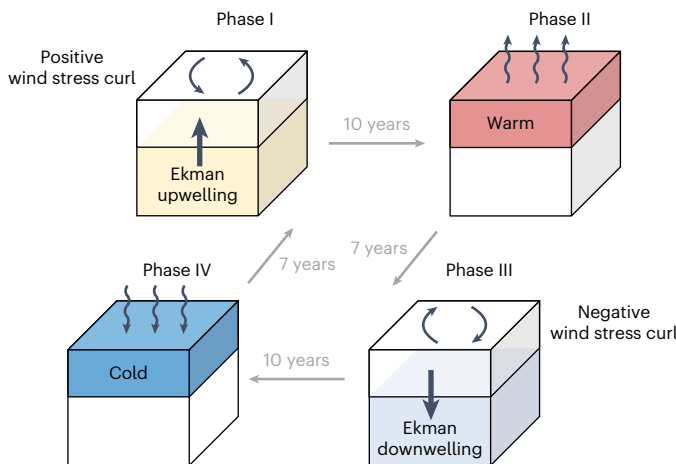


Fig. 3 | Changes in the Arctic surface temperature anomaly across the LongRunMIP ensembles. **a**, The multitaper spectra of 39 LongRunMIP simulations are compiled with their corresponding GMST levels. The multitaper spectrum for each simulation is shown in Extended Data Fig. 2. The power spectrum is averaged for five different GMST ranges: $12^{\circ}\text{C} < \text{GMST} \leq 15^{\circ}\text{C}$ (blue line), $15^{\circ}\text{C} < \text{GMST} \leq 18^{\circ}\text{C}$ (sky blue line), $18^{\circ}\text{C} < \text{GMST} \leq 21^{\circ}\text{C}$ (yellow line), $21^{\circ}\text{C} < \text{GMST} \leq 24^{\circ}\text{C}$ (orange line) and $24^{\circ}\text{C} < \text{GMST}$ (red line). The black dashed line indicates the 99% confidence level against the red noise null hypothesis. **b**, The relationship between AC1 and GMST for 39 LongRunMIP simulations. Each dot indicates a LongRunMIP simulation, with the colour denoting its annual mean sea-ice area. Simulations that exhibit a practically ice-free summer state (sea-ice area less than 10^6 km^2) are marked with a cross. The black line is the fitted line of the AC1–GMST relationship using a shifted power function. The AC1 for each simulation is shown in Extended Data Fig. 8.

The altered surface temperature would again induce the change in the wind stress curl. The wind stress curl shows a nearly in-phase relationship with the Laplacian of negative surface temperature (that is, $-\nabla^2 T$, where T is surface temperature) (Extended Data Fig. 5c), consistent with the result from the marine atmospheric boundary layer model²⁴ (Methods). The Laplacian of temperature shows lagged change to the temperature with 6 years (Extended Data Fig. 5d) due to the spatial pattern of the oscillation (Extended Data Fig. 6c,d). These are physically interpreted as follows: a warm (cold) surface temperature induces negative (positive) Laplacian of surface temperature and results in negative (positive) wind stress curl anomaly.

These time-lagged dynamical responses form four phases of an oscillation cycle: positive wind stress curl (phase I), warm surface (phase II), negative wind stress curl (phase III) and cold surface (phase IV). This feedback loop is schematically summarized in Fig. 4. The reconstructed oscillation period based on the lead–lag analysis is 34 years, almost identical to the spectral peak period of 36 years. The proposed oscillation mechanism is a unique process that can occur only in the polar ocean featuring an inversion in the vertical temperature profile (increasing temperature with depth). The Ekman advection feedback would oppositely occur in non-polar oceans with a regular vertical temperature profile (decreasing temperature with depth), and thus the oscillation loop cannot occur.

To further validate the proposed oscillation mechanism, we conduct the multitaper method–singular value decomposition



(MTM–SVD) analysis on the global joint surface temperature–wind stress curl field (Methods). The MTM–SVD analysis consistently reconstructs the proposed oscillation mechanism. The joint oscillatory mode of surface temperature–wind stress curl is uniquely detected in the Arctic Ocean, with a spectral peak of 33 years above a 99% confidence level (Extended Data Fig. 7a). The reconstructed surface temperature for the period of 33 years displays a stationary monopole oscillation pattern (Extended Data Fig. 7c) and shows 7.5 years lag to wind stress curl (Extended Data Fig. 7e). The proposed oscillation mechanism is also consistently found in the MPI-ESM1.2 abrupt4x experiment (Supplementary Figs. 2 and 3).

Conceptual model for the oscillation

Synthesizing the mechanisms, we introduce a conceptual model for the oscillation (Methods and Supplementary Discussions 2–4). The model considers the interplay between surface temperature and wind stress curl as a coupled oscillator of these two variables—surface temperature and wind stress curl—and links their coupling strength to the GMST level. This linkage between the coupling strength and GMST represents the intensified air–sea interaction processes due to the sea-ice area decrease in a warming climate. The model features the Hopf bifurcation point, a critical threshold that gives birth to periodic oscillation in a dynamical system^{25,26}. We set the Hopf bifurcation point as a GMST level of 16.5°C on the basis of the CMIP6 analysis results (Fig. 2) and demonstrate changes in surface temperature variability under increasing GMST (Fig. 5). When the GMST is below 16.5°C , the surface temperature variability is driven mainly by climate noise and does not show a clear spectral peak. As the GMST increases and surpasses 16.5°C , the internal oscillation dynamic activates and begins to drive the periodic oscillation mode of the surface temperature. The conceptual model reproduces the emergence of the periodic oscillation mode and consistently explains the CMIP6 and LongRunMIP results.

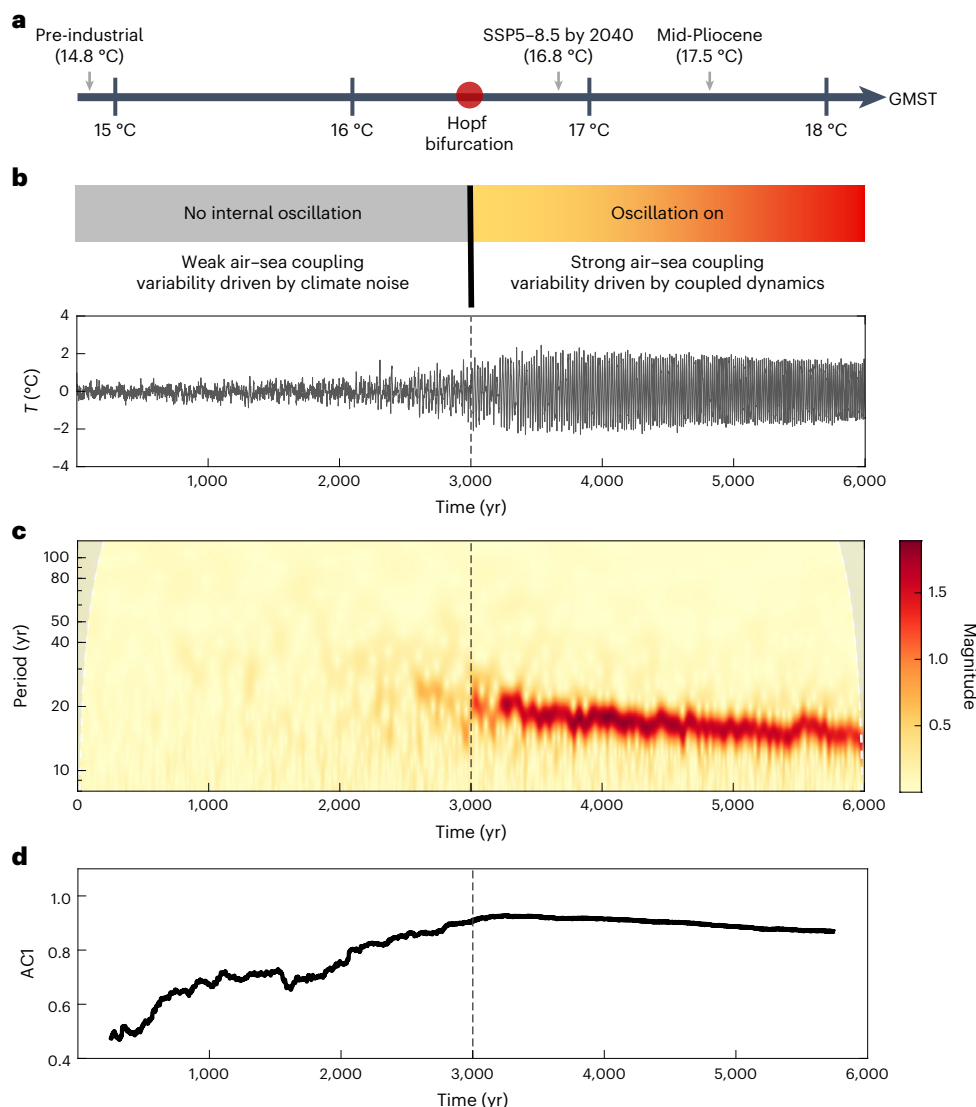


Fig. 5 | The conceptual model for the critical transition of the Arctic surface temperature variability. The critical transition in the surface temperature variability pattern is demonstrated using the conceptual model (Methods). The GMST is linearly increased at a rate of 3.4 °C per 6,000 years. **a**, The key GMST levels of past and future climates. **b**, The time series of the surface temperature.

When the GMST passes the critical threshold at 16.5 °C in the year 3000 (the so-called Hopf bifurcation point), the variability pattern of surface temperature changes from a random-like to a periodic fluctuation pattern. **c**, Wavelet power spectrum of the surface temperature. **d**, The 500-year moving AC1 of the surface temperature.

Early warning signals in the observation

If the Arctic Ocean is currently approaching the critical threshold, the early warning signal of the oscillation emergence would be detected in the observational record. We use the lag-1 autocorrelation (AC1), a robust early warning indicator for the Hopf bifurcation^{27–29}, to detect the early warning signal. The use of AC1 as an early warning indicator is based on the critical slowing-down theory and has been extensively tested and used in previous studies^{27–31}. The increase in AC1 can be directly interpreted as a slower recovery from perturbations (slower dynamics), implying that the low-frequency dynamics become more dominant in the variability. The increasing trend in AC1 is consistently found in the majority of CMIP6 models (Fig. 2c), LongRunMIP simulations (Fig. 3b and Extended Data Fig. 8) and the conceptual model (Fig. 5d) (note that changing trend is a meaningful indicator, not the value itself). These consistent responses show that AC1 is a reliable indicator for early warning of the oscillation emergence and to confirm that the slowing down of variability robustly occurs by increasing warming. Note that, physically, the AC1 is not affected only by the air-sea coupling strength, but also by other factors such as stochastic

weather noise and the thermal inertia of the Arctic Ocean. Therefore, a temporal decrease of AC1 can naturally occur due to other factors, even if the increasing air-sea coupling continuously pushes the Arctic Ocean to the threshold of oscillation emergence (for example, a temporary decrease of the CMIP6 ensemble mean AC1 in 1950).

We use four in situ surface temperature observation records: the Met Office Hadley Centre/Climate Research Unit version 5 (HadCRUT5)³², the National Oceanic and Atmospheric Administration Merged Land Ocean Global Surface Temperature Analysis version 5 (NOAAGlobalTemp5)³³, NASA's (National Aeronautics and Space Administration's) Goddard Institute for Space Studies Surface Temperature version 4 (GISTEMP4)³⁴ and the Berkeley Earth temperature dataset (BerkeleyEarth)³⁵ (Methods). The significant continuous increasing trend in AC1 during 1920–2021 is detected in three observational records, HadCRUT5, NOAAGlobalTemp5 and GISTEMP4 (Extended Data Fig. 9). As an exception, BerkeleyEarth shows an insignificant trend during the recent decades. These show that the AC1 early warning signal of the oscillation emergence is found in the majority of the observational records and supports our results from the climate model simulations.

Implication in the Pliocene

The emergence of the oscillation in the warm climates implies that the oscillation might have existed in the past warm climate. The Pliocene, the epoch 5.3 to 2.5 million years before the present, was 1.8 °C to 3.6 °C warmer than the pre-industrial period and provides the best analogue for the future warm climate³⁶. The analysis of the mid-Pliocene simulations from the PlioMIP2 (Methods) shows that 6 out of 13 models (13 out of 13 models) exhibit a multidecadal spectral peak over the 99% (95%) confidence level against climate noise (Extended Data Fig. 10a). The model with a strong spectral peak above the 99% confidence level shows a significantly warmer Arctic climate state than other models, supporting our oscillation emergence hypothesis (Extended Data Fig. 10b). It implies that the oscillation might have existed in the past warm climate. A further palaeo-proxy record analysis is required to confirm the presence of the oscillation.

Discussions

Our findings suggest that the sea-ice loss by global warming can cause a critical transition in temperature fluctuation patterns, triggering a novel climate oscillation mode in the Arctic. This oscillation occurs due to a unique feature of the upper Arctic Ocean, where ocean temperature increases with depth. Given the far-reaching teleconnection impacts of the Arctic climate^{37–43}, the emerging oscillation in a warmer climate could potentially have a considerable effect on the global weather and climate. These implications should be further investigated in further studies.

There are other characteristics of the oscillation that need further study. First, the emerging oscillation is quasi-periodic, featuring multiple spectral peaks and broad spectra (for example, Extended Data Fig. 3c). These are typical characteristics found in other climate oscillations such as the El Niño/Southern Oscillation⁴⁴ and the Indian Ocean Dipole⁴⁵. These can be caused by nonlinear effects (for example, frequency cascading^{46,47} and resonance^{48,49}) or by stochastic weather forcing⁵. Second, the dynamical mechanism and conceptual model of the oscillation imply that the characteristics of the oscillation, such as period and amplitude, can be modulated depending on the background state of the Arctic Ocean. For example, the CMIP6 wavelet analysis shows a shift in the spectral peak from 14 to 18 years (Fig. 2b), implying that the modulation is caused by the change in the background Arctic environment.

Our results are based mainly on climate model simulations. The CMIP6 and LongRunMIP models simulate the Arctic climate and its variability reasonably well, but with some biases (Supplementary Discussions 5 and 6). This implies that there may be biases in the emergence timing and characteristics of the oscillation. A follow-up simulation using a finely tuned model focusing on the central Arctic Ocean is required.

Online content

Any methods, additional references, Nature Portfolio reporting summaries, source data, extended data, supplementary information, acknowledgements, peer review information; details of author contributions and competing interests; and statements of data and code availability are available at <https://doi.org/10.1038/s41558-024-02171-3>.

References

1. Davy, R. & Outten, S. The Arctic surface climate in CMIP6: status and developments since CMIP5. *J. Clim.* **33**, 8047–8068 (2020).
2. Rantanen, M. et al. The Arctic has warmed nearly four times faster than the globe since 1979. *Commun. Earth Environ.* **3**, 168 (2022).
3. Wunderling, N., Willeit, M., Donges, J. F. & Winkelmann, R. Global warming due to loss of large ice masses and Arctic summer sea ice. *Nat. Commun.* **11**, 5177 (2020).
4. Notz, D. SIMIP Community Arctic sea ice in CMIP6. *Geophys. Res. Lett.* **47**, e2019GL086749 (2020).
5. Jin, F.-F. An equatorial ocean recharge paradigm for ENSO. Part I: conceptual model. *J. Atmos. Sci.* **54**, 811–829 (1997).
6. Li, T., Wang, B., Chang, C.-P. & Zhang, Y. A theory for the Indian Ocean Dipole–zonal mode. *J. Atmos. Sci.* **60**, 2119–2135 (2003).
7. Deser, C., Alexander, M. A., Xie, S.-P. & Phillips, A. S. Sea surface temperature variability: patterns and mechanisms. *Ann. Rev. Mar. Sci.* **2**, 115–143 (2010).
8. Thompson, D. W. J. & Wallace, J. M. The Arctic oscillation signature in the wintertime geopotential height and temperature fields. *Geophys. Res. Lett.* **25**, 1297–1300 (1998).
9. Polyakov, I. V. et al. Variability and trends of air temperature and pressure in the maritime Arctic, 1875–2000. *J. Clim.* **16**, 2067–2077 (2003).
10. van der Linden, E. C., Bintanja, R., Hazeleger, W. & Graversen, R. G. Low-frequency variability of surface air temperature over the Barents Sea: causes and mechanisms. *Clim. Dyn.* **47**, 1247–1262 (2016).
11. Deng, J. & Dai, A. Sea ice–air interactions amplify multidecadal variability in the North Atlantic and Arctic region. *Nat. Commun.* **13**, 2100 (2022).
12. Luo, B. et al. Origins of Barents–Kara sea-ice interannual variability modulated by the Atlantic pathway of El Niño–Southern Oscillation. *Nat. Commun.* **14**, 585 (2023).
13. Luo, D., Chen, X., Dai, A. & Simmonds, I. Changes in atmospheric blocking circulations linked with winter Arctic warming: a new perspective. *J. Clim.* **31**, 7661–7678 (2018).
14. Screen, J. A., Bracegirdle, T. J. & Simmonds, I. Polar climate change as manifest in atmospheric circulation. *Curr. Clim. Change Rep.* **4**, 383–395 (2018).
15. Polyakov, I. V. et al. Recent oceanic changes in the Arctic in the context of long-term observations. *Ecol. Appl.* **23**, 1745–1764 (2013).
16. Polyakov, I. et al. Trends and variations in Arctic Climate System. *Eos* **83**, 547–548 (2002).
17. Polyakov, I., Walsh, D., Dmitrenko, I., Colony, R. L. & Timokhov, L. A. Arctic Ocean variability derived from historical observations. *Geophys. Res. Lett.* **30**, 1298 (2003).
18. Eyring, V. et al. Overview of the Coupled Model Intercomparison Project Phase 6 (CMIP6) experimental design and organization. *Geosci. Model. Dev.* **9**, 1937–1958 (2016).
19. O'Neill, B. C. et al. The Scenario Model Intercomparison Project (ScenarioMIP) for CMIP6. *Geosci. Model. Dev.* **9**, 3461–3482 (2016).
20. Rugenstein, M. et al. LongRunMIP: motivation and design for a large collection of millennial-length AOGCM simulations. *Bull. Am. Meteorol. Soc.* **100**, 2551–2569 (2019).
21. Haywood, A. M. et al. The Pliocene Model Intercomparison Project (PlioMIP) phase 2: scientific objectives and experimental design. *Clim. Past* **12**, 663–675 (2016).
22. Weiffenbach, J. E. et al. Unraveling the mechanisms and implications of a stronger mid-Pliocene Atlantic Meridional Overturning Circulation (AMOC) in PlioMIP2. *Clim. Past* **19**, 61–85 (2023).
23. de Nooijer, W. et al. Evaluation of Arctic warming in mid-Pliocene climate simulations. *Clim. Past* **16**, 2325–2341 (2020).
24. Minobe, S., Kuwano-Yoshida, A., Komori, N., Xie, S.-P. & Small, R. J. Influence of the Gulf Stream on the troposphere. *Nature* **452**, 206–209 (2008).
25. Hassard, B. D., Kazarinoff, N. D. & Wan, Y.-H. *Theory and Applications of Hopf Bifurcation* Vol. 41 (Cambridge Univ. Press, 1981).
26. Jiménez-Ramírez, O., Cruz-Domínguez, E. J., Quiroz-Juárez, M. A., Aragón, J. L. & Vázquez-Medina, R. Experimental detection of Hopf bifurcation in two-dimensional dynamical systems. *Chaos Solitons Fractals X* **6**, 100058 (2021).

27. Tirabassi, G. & Masoller, C. Correlation lags give early warning signals of approaching bifurcations. *Chaos Solitons Fractals* **155**, 111720 (2022).
28. Dutta, P. S., Sharma, Y. & Abbott, K. C. Robustness of early warning signals for catastrophic and non-catastrophic transitions. *Oikos* **127**, 1251–1263 (2018).
29. Ghanavati, G., Hines, P. D. H. & Lakoba, T. I. Investigating early warning signs of oscillatory instability in simulated phasor measurements. In *Proc. 2014 IEEE PES General Meeting | Conference & Exposition 1–5* (Institute of Electrical and Electronics Engineers, 2014); <https://doi.org/10.1109/PESGM.2014.6939263>
30. Nazarimehr, F., Jafari, S., Perc, M. & Sprott, J. C. Critical slowing down indicators. *Europhys. Lett.* **132**, 18001 (2020).
31. Scheffer, M. et al. Early-warning signals for critical transitions. *Nature* **461**, 53–59 (2009).
32. Morice, C. P. et al. An updated assessment of near-surface temperature change from 1850: the HadCRUT5 data set. *J. Geophys. Res. Atmos.* **126**, e2019JD032361 (2021).
33. Vose, R. S. et al. Implementing full spatial coverage in NOAA's global temperature analysis. *Geophys. Res. Lett.* **48**, e2020GL090873 (2021).
34. Lenssen, N. J. L. et al. Improvements in the GISTEMP uncertainty model. *J. Geophys. Res. Atmos.* **124**, 6307–6326 (2019).
35. Rohde, R. A. & Hausfather, Z. The Berkeley Earth Land/Ocean temperature record. *Earth Syst. Sci. Data* **12**, 3469–3479 (2020).
36. Burke, K. D. et al. Pliocene and Eocene provide best analogs for near-future climates. *Proc. Natl Acad. Sci. USA* **115**, 13288–13293 (2018).
37. Kug, J.-S. et al. Two distinct influences of Arctic warming on cold winters over North America and East Asia. *Nat. Geosci.* **8**, 759–762 (2015).
38. Cohen, J., Pfeiffer, K. & Francis, J. A. Warm Arctic episodes linked with increased frequency of extreme winter weather in the United States. *Nat. Commun.* **9**, 869 (2018).
39. Coumou, D., Di Capua, G., Vavrus, S., Wang, L. & Wang, S. The influence of Arctic amplification on mid-latitude summer circulation. *Nat. Commun.* **9**, 2959 (2018).
40. Cohen, J. et al. Divergent consensuses on Arctic amplification influence on midlatitude severe winter weather. *Nat. Clim. Change* **10**, 20–29 (2020).
41. Zhuo, W., Yao, Y., Luo, D., Simmonds, I. & Huang, F. The key atmospheric drivers linking regional Arctic amplification with East Asian cold extremes. *Atmos. Res.* **283**, 106557 (2023).
42. Rudeva, I. & Simmonds, I. Midlatitude winter extreme temperature events and connections with anomalies in the Arctic and tropics. *J. Clim.* **34**, 3733–3749 (2021).
43. Luo, D., Yao, Y., Dai, A., Simmonds, I. & Zhong, L. Increased quasi stationarity and persistence of winter Ural blocking and Eurasian extreme cold events in response to Arctic warming. Part II: a theoretical explanation. *J. Clim.* **30**, 3569–3587 (2017).
44. Timmermann, A. et al. El Niño–Southern Oscillation complexity. *Nature* **559**, 535–545 (2018).
45. Stuecker, M. F. et al. Revisiting ENSO/Indian Ocean Dipole phase relationships. *Geophys. Res. Lett.* **44**, 2481–2492 (2017).
46. Stuecker, M. F., Timmermann, A., Jin, F.-F., McGregor, S. & Ren, H.-L. A combination mode of the annual cycle and the El Niño–Southern Oscillation. *Nat. Geosci.* **6**, 540–544 (2013).
47. Stuecker, M. F., Jin, F.-F. & Timmermann, A. El Niño–Southern Oscillation frequency cascade. *Proc. Natl Acad. Sci. USA* **112**, 13490–13495 (2015).
48. Jin, F.-F., Neelin, J. D. & Ghil, M. El Niño on the Devil's Staircase: annual subharmonic steps to chaos. *Science* **264**, 70–72 (1994).
49. Tziperman, E., Stone, L., Cane, M. A. & Jarosh, H. El Niño chaos: overlapping of resonances between the seasonal cycle and the Pacific ocean-atmosphere oscillator. *Science* **264**, 72–74 (1994).

Publisher's note Springer Nature remains neutral with regard to jurisdictional claims in published maps and institutional affiliations.

Open Access This article is licensed under a Creative Commons Attribution-NonCommercial-NoDerivatives 4.0 International License, which permits any non-commercial use, sharing, distribution and reproduction in any medium or format, as long as you give appropriate credit to the original author(s) and the source, provide a link to the Creative Commons licence, and indicate if you modified the licensed material. You do not have permission under this licence to share adapted material derived from this article or parts of it. The images or other third party material in this article are included in the article's Creative Commons licence, unless indicated otherwise in a credit line to the material. If material is not included in the article's Creative Commons licence and your intended use is not permitted by statutory regulation or exceeds the permitted use, you will need to obtain permission directly from the copyright holder. To view a copy of this licence, visit <http://creativecommons.org/licenses/by-nc-nd/4.0/>.

© The Author(s) 2024

Methods

The CMIP6 archive

We use historical and SSP5–8.5 experiment output from the CMIP6 archive^{18,19}. We use all 41 models that consistently provide surface temperature variables for both historical and SSP5–8.5 experiments. The model names and ensemble types are presented in Supplementary Table 1. The most typical ensemble type is ‘r1i1p1f1’, but a different type is used when it is not available. We merged the historical experiment (1850–2014) and SSP5–8.5 experiment (2015–2099) for each of the 41 models. The total length of the merged historical and SSP5–8.5 simulation is 250 years (1850–2099). We also use the piControl experiment to provide a confidence level for the wavelet analysis. The piControl analysis uses the same model and ensemble type as the historical/SSP5–8.5. As an exception, the CESM2, HadCM3-GC31-LL and MCM-UA-1-0 use a different ensemble type with the historical/SSP5–8.5, because their same ensemble type simulations with the historical/SSP5–8.5 are not publicly available. These differences in ensemble type do not affect the comparison between piControl and historical/SSP5–8.5 simulations as the difference in ensemble type is due only to differences in initial conditions.

The LongRunMIP archive

We use a total of 39 simulation runs from 13 models from the LongRunMIP archive²⁰. The LongRunMIP analysis sample includes 13 control experiments and 26 high-CO₂ experiments. The typical high-CO₂ experiments are the abrupt2x, abrupt4x and abrupt8x, which simulate forcing scenarios of instantaneous doubling, quadrupling and octupling of atmospheric CO₂ level, respectively (19 out of 26 high-CO₂ experiments run). After the abrupt increase in CO₂ level, the forcing is stabilized for longer than 1,000 years. The abrupt700ppm and abrupt1400ppm experiments from CCSM3II simulate a linear increase in CO₂ level for 90 years until it reaches 2.4 and 4.8 times, respectively (2 out of 26 high-CO₂ experiments run). The 1pct2x and 1pct4x experiments from GFDL-CM3, GFDL-ESM2M, MIROC 3.2 and GISS-E2-R simulate a gradual increase in CO₂ level with a rate of 1% per year until it reaches doubled and quadrupled levels, respectively (5 out of 26 high-CO₂ experiments run). We specifically use the last 1,000 years of the simulations where the GMST sufficiently reaches a quasi-equilibrium state. A similar approach was adopted in ref. 50. As an exception, some models are selected for less than 1,000 years due to their short simulation length, but all of them are longer than 500 years. The exceptions are HadCM3L, MPI-ESM12, CNRMCM61, IPSLCM5A and MIROC32. The model name, experiment, total and selected length of the simulation are listed in Supplementary Table 2. The details of the model set-up and experiment protocol can be found in ref. 20.

The PlioMIP2 archive

We use the control Pliocene experiment (EoI⁴⁰⁰) from the PlioMIP2 archive²¹. The EoI⁴⁰⁰ simulates the mid-Pliocene climate (3.3 to 3.0 million years before the present) using the boundary conditions of the Pliocene ice sheets and orography with an atmospheric CO₂ level of 400 ppm. We use 13 models. A typical length of the simulation is 100 years, but some models (CESM 1.0.5, CESM2 and EC-Earth3-LR) simulate longer lengths. The model name, total and selected length of the simulation for analysis are listed in Supplementary Table 3. The details of the model set-up and experiment configuration can be found in ref. 21.

The observation data

We use four in situ surface temperature anomaly records: HadCRUT5³², NOAAGlobalTemp5³³, GISTEMP4³⁴ and BerkeleyEarth³⁵. We use records for 1920–2021.

Calculation of the Arctic surface temperature anomaly

We calculate the Arctic surface temperature anomaly for the CMIP6, LongRunMIP and PlioMIP2. Surface temperature (model output

variable name: ‘ts’) is the skin temperature at the ground level (for example, land surface temperature on land, and sea surface temperature on the ocean). All surface temperature data are in rectangular grid format. We first calculate the area-averaged annual surface temperature for the central Arctic Ocean (80° N–90° N). Then, we calculate its anomaly by subtracting its climatology for the entire given period. We applied quadratic detrending to remove the background warming trend, which is well approximated by the quadratic function (Fig. 1b).

Calculation of the upper Arctic Ocean temperature anomaly

We calculate the upper Arctic Ocean temperature anomaly for CMIP6 data. We use 5 m ocean temperature. We first calculate the area-averaged 5 m ocean temperature for the Arctic Ocean (80° N–90° N). To calculate its anomaly, we apply the exact same routine used for the Arctic surface temperature anomaly calculation. Two models (AWI-CM-1-1-MR and IITM-ESM) are not included in the calculation because of their unavailability.

Calculation of the Arctic sea-ice area

We calculate the Arctic sea-ice area for each ensemble member of the CMIP6 and LongRunMIP. There are two commonly used indicators for measuring sea-ice coverage: sea-ice area and sea-ice extent. We use sea-ice area here because it provides a direct representation of the total region covered by ice and is therefore more closely related to the strength of the air–sea interaction processes. We calculate the annual mean and summer sea-ice area. The summer sea-ice area is defined as the sea-ice area in September, which is the calendar month with the minimum amount of sea ice. We sum the sea-ice area over the entire Northern Hemisphere (0° N–90° N) to obtain the total sea-ice area. Four models (AWI-CM-1-1-MR, GISS-ER-1-G, IITM-ESM and MCM-UA-1-0) are not included in the calculation because of their unavailability.

Multitaper spectral analysis

We perform the multitaper spectral analysis on the surface temperature anomaly time series. The multitaper method is a widely used technique for power spectrum estimation⁵¹. The multitaper method is based on a small set of tapers, each giving different weighting to the time series. The multitaper power spectrum is obtained from the average of the power spectrums from each taper. This averaging process provides a more accurate and robust estimation of the power spectrum compared with traditional methods such as periodogram. The analysis is performed with the time–frequency bandwidth parameter (NW) of 2, and the number of Slepian tapers (*K*) of 3. This choice of parameters gives optimal resistance to spectral leakage. We determine the confidence level of the power spectrum on the basis of the red noise, which is a typical null hypothesis for climate variability⁵². We estimate the confidence level using the Monte Carlo approach with 1,000 ensembles. These confidence levels provide a baseline for how confidently the power spectrum can be distinguished from background climate noise. We perform the multitaper spectrum analysis for multiple ensemble members for the CMIP6, LongRunMIP and PlioMIP2 archives. To make the power spectrums comparable within a single figure, we normalized the power spectrum to have the same relative distance to the confidence level, following ref. 53. Therefore, the relative distance between the confidence level and spectral power remains unchanged after the normalization, even if the absolute level is different from the raw spectrum.

Wavelet analysis

We perform wavelet analysis on the surface temperature anomaly of the merged historical and SSP5–8.5 experiments from the CMIP6 archive. We use the Morse and Morlet wavelets, two of the most commonly used wavelet functions. These wavelet functions are known to have a good balance between time and frequency resolution.

The voice per octave of wavelet is set to 48. To provide a confidence line for the wavelet power spectrum, we calculate the wavelet power for the piControl experiment, a fixed forcing run with the 1850 condition. We calculate the mean + 1 s.d. and mean + 2 s.d. levels of the piControl experiment wavelet power and use these levels as the baseline. This piControl confidence line shows how significantly the wavelet power spectrum changed from the fixed 1850 condition.

AC1 analysis

We calculate the AC1 of the annual surface temperature anomaly for the CMIP6, LongRunMIP and observational datasets.

MTM–SVD analysis

We perform MTM–SVD analysis on the CESM 1.0.4 abrupt4x experiment of the LongRunMIP archive. MTM–SVD is essentially a combination of multitaper spectral analysis (which is previously introduced) and singular value decomposition⁵⁴. MTM–SVD can reliably detect a spatially coherent oscillatory signal at a narrow band of spectral frequency from the given climate field data consisting of space and time domains. We perform joint MTM–SVD analysis on the global anomaly field of surface temperature and wind stress curl. Note that, for the input, we use the global domain instead of the Arctic region to examine whether the oscillation mode exclusively manifests in the Arctic region. We perform the MTM–SVD analysis following the standard routine outlined in refs. 53,54. We set the time–frequency bandwidth parameter (NW) to 2 and the number of Slepian tapers (K) to 3. The outputs of the MTM–SVD analysis are the local fractional variance (LFV) spectrum and the reconstructed oscillation signal at desired frequency f . LFV is a signal detection parameter that indicates whether there is a single spatially coherent oscillatory signal at the desired frequency f (detailed explanations can be found in ref. 54). The confidence level of the LFV spectrum is determined on the basis of the red noise null hypothesis⁵². We estimate the confidence level using the Monte Carlo approach with 1,000 ensembles. The obtained LFV spectrum is presented in Extended Data Fig. 7a. MTM–SVD can reconstruct the signal with a frequency centred at f with a bandwidth of $\pm pf_R$, where f_R is the Rayleigh frequency (the minimum resolvable frequency) and $p = K - 1$. We reconstruct the oscillation at frequency $f = 1/33 \text{ yr}^{-1}$ where its LFV exceeds the 99% confidence level. The reconstructed surface temperature and wind stress curl anomalies are presented in Extended Data Fig. 7b–e. Note that the reconstruction is performed over a very narrow frequency range ($\pm pf_R$), thus the absolute magnitude of the reconstructed physical variables can be small.

Ekman advection analysis

We perform Ekman advection analysis using the CESM 1.0.4 abrupt4x experiment of the LongRunMIP archive. This abrupt4x experiment features the surface temperature anomaly spectral peak period of 36 years (Extended Data Fig. 3c). We band-pass filtered all physical variables for a period range of 30–40 years to facilitate the analysis. The time evolution of surface temperature, ocean temperature with depth, Laplacian of sea surface temperature and wind stress curl on ocean surface during years 712–738 are presented in Extended Data Fig. 6. The physical assumption on the Ekman advection analysis can be found in Supplementary Discussion 1.

The temperature advection by the Ekman transport ($\frac{\partial T_E}{\partial t}$) is calculated by:

$$\frac{\partial T_E}{\partial t} = -u_E \frac{\partial \bar{T}}{\partial x} - v_E \frac{\partial \bar{T}}{\partial y} - w_E \frac{\partial \bar{T}}{\partial z} - \bar{u}_E \frac{\partial T}{\partial x} - \bar{v}_E \frac{\partial T}{\partial y} - \bar{w}_E \frac{\partial T}{\partial z} \quad (1)$$

where

$$u_E = \frac{\sqrt{2}}{\rho_0 f d} e^{z/d} \left[\bar{r}^x \cos\left(\frac{z}{d} - \frac{\pi}{4}\right) - \bar{r}^y \sin\left(\frac{z}{d} - \frac{\pi}{4}\right) \right] \quad (2)$$

$$v_E = \frac{\sqrt{2}}{\rho_0 f d} e^{z/d} \left[\bar{r}^x \sin\left(\frac{z}{d} - \frac{\pi}{4}\right) + \bar{r}^y \cos\left(\frac{z}{d} - \frac{\pi}{4}\right) \right] \quad (3)$$

$$w_E = \frac{1}{\rho_0 f} \left[-(\nabla \cdot \bar{\tau}) e^{z/d} \sin\left(\frac{z}{d}\right) + (\nabla \times \bar{\tau})_z \left(1 - e^{z/d} \cos\left(\frac{z}{d}\right)\right) \right]. \quad (4)$$

Here u_E , v_E and w_E are anomalous zonal, meridional and vertical Ekman velocities, respectively; \bar{r}^x and \bar{r}^y are anomalous zonal and meridional wind stresses, respectively; $\bar{\tau} = (\bar{r}^x, \bar{r}^y, 0)$; and T is anomalous ocean temperature. The overbar (\bar{x}) denotes its time mean quantity (for example, \bar{T} is the mean ocean temperature); ρ_0 is the ocean density, f is the Coriolis parameter, d is the Ekman depth, and z is the ocean depth. The parameters are set to $\rho_0 = 1,000 \text{ kg m}^{-3}$, $f = 1.43 \times 10^{-4} \text{ rad s}^{-1}$ (the value at latitude 80° N), and $d = 20 \text{ m}$ (ref. 55). The Ekman depth depends on the latitude and the strength of the vertical mixing process (Supplementary Discussion 1), but we assume it is constant for simplicity. We use \bar{r}^x , \bar{r}^y and T from the simulation output to calculate the Ekman advection terms. For each grid point of the simulation output (longitude, latitude and depth), the Ekman advection terms (right-hand side of equation (1)) are calculated. Then, a three-dimensional box average is performed for 80° N – 90° N and 0 m–300 m. The standard deviations of the calculated Ekman advection terms are shown in Extended Data Fig. 4a. The lead–lag correlation between the ocean temperature tendency ($\frac{\partial T}{\partial t}$) is shown in Extended Data Fig. 4b.

The main results of the standard deviation and lead–lag correlation analysis are unchanged even when we use the unfiltered raw physical variables (Supplementary Fig. 4). The reason we band-pass filter the physical variables is to maintain consistency between the lead–lag correlation analyses, which strictly requires the band-pass filtering process. A detailed explanation can be found in the next subsection.

The vertical resolution of CESM 1.0.4 is 10 m (ref. 56), which is relatively coarse compared with the Ekman depth. Therefore, the spatial pattern of the Ekman spiral structure may not be well represented in the model output. However, our main focus of the analysis is to calculate the spatially averaged Ekman advection caused by the Ekman current rather than the Ekman current itself. Therefore, the relatively coarse vertical resolution of the model would not notably affect the analysis (CESM 1.0.4 uses a second-order central advection scheme for ocean⁵⁶). Note that the raw annual ocean current variables are not available from the simulation output because they are not included in the core variable of the LongRunMIP protocol²⁰.

Lead–lag correlation analysis

We perform a series of lead–lag correlation analyses for the CESM 1.0.4 abrupt4x experiment of the LongRunMIP archive. We band-pass filtered all physical variables for a period range of 30–40 years. We use the area-averaged surface temperature, surface temperature tendency and wind stress curl over the Arctic (80° N – 90° N) to investigate the response of surface temperature to wind stress curl change. We analyse the lead–lag correlation between wind stress curl and surface temperature tendency (Extended Data Fig. 5a) and wind stress curl and surface temperature (Extended Data Fig. 5b). We use the area-averaged surface temperature, surface temperature Laplacian and wind stress curl over the Arctic (70° N – 90° N) to investigate the response of wind stress curl to surface temperature change. We here extend the southern edge of the average area from 80° N to 70° N to fully consider the wind stress variation pattern, given that the maximum wind field response position is typically displaced from the surface temperature change centre⁵⁷. We analyse the lead–lag correlation between the surface temperature Laplacian and wind stress curl (Extended Data Fig. 5c) and the surface temperature Laplacian and surface temperature (Extended Data Fig. 5d).

Band-pass filtering is an essential pre-processing step for lead–lag correlation analysis because the oscillation has multiple spectral peaks.

The physical interpretation of the lead–lag correlation results implicitly assumes that the oscillation has a single peak frequency. This allows us to translate the lead–lag correlation (a sign of peak correlation and lead/lag of peak correlation) into physical information about the oscillation mechanism (interplay between surface temperature–wind stress curl and duration of phase transition). When multiple frequencies are involved, these physical interpretations cannot provide unique and reliable physical information because multiple physical interpretations are possible from the lead–lag correlation. Since the oscillation is quasi-periodic and has multiple peaks (for example, 48 years) (Extended Data Fig. 2c), band-pass filtering is an essential pre-process to obtain valid physical interpretations from the lead–lag correlation analysis. The main physical results remain unchanged even when we perform the analysis with band-pass filtered variables for the period range of 40–50 years (Supplementary Fig. 5).

Marine atmospheric boundary layer model

The atmospheric marine boundary layer model²⁴ is given as:

$$\varepsilon u - fv = -p_x/\rho_a \quad (5)$$

$$\varepsilon v + fu = -p_y/\rho_a \quad (6)$$

$$\varepsilon p + H(u_x + v_y) = -\gamma T. \quad (7)$$

where p_x and p_y are zonal and meridional atmospheric pressure gradients, respectively; u and v are zonal and meridional surface wind velocities, respectively; T is sea surface temperature; ε is the damping parameter, f is the Coriolis parameter, ρ_a is the air density, H is equivalent depth and γ is the sensitivity parameter. The relationship between the wind velocity curl and sea surface temperature Laplacian is written approximately as follows by ignoring high-order gradients:

$$(\nabla \times \mathbf{u})_z = \frac{1}{\varepsilon^2 + f^2} \frac{f}{\varepsilon} \frac{\gamma}{\rho_a} (-\nabla^2 T) \quad (8)$$

where $\mathbf{u} = (u, v, 0)$ and subscript z denotes the vertical component. This equation shows that the vertical component of the wind velocity curl is proportional to the negative sea surface temperature Laplacian. Since the wind stress is proportional to the square of wind velocity, the wind stress curl is approximately proportional to the negative sea surface temperature Laplacian, $(\nabla \times \tau)_z \propto -\nabla^2 T$.

Conceptual model for the oscillation

We introduce the conceptual model for the oscillation. The model incorporates the interplay between surface temperature and wind stress curl as a coupled oscillator of two variables. The detailed derivation of the model can be found in Supplementary Discussion 2. The model is written as follows:

$$\frac{dT}{dt} = -\beta T + \alpha x - eT^3 + \sigma_T \xi_T \quad (9)$$

$$\frac{dx}{dt} = -\gamma T - \varepsilon x + \sigma_x \xi_x. \quad (10)$$

where T and x are the surface temperature and wind stress curl anomaly, respectively; αx describes surface temperature change by the vertical Ekman advection process (transition from phase I to II and from III to IV) and $-\gamma T$ parameterizes the wind stress curl change by surface temperature (transition from phase II to III and from IV to I); $-\beta T$ and $-\varepsilon x$ represent damping; $-eT^3$ is the cubic surface temperature instability that enables stable sustainability of the oscillation over a wide range of parameters by prohibiting unstable infinite growth of the system.

The model also includes stochastic forcing for surface temperature ($\sigma_T \xi_T$) and wind stress curl ($\sigma_x \xi_x$); ξ_T and ξ_x are the white noise with zero mean and unit variance; σ_T and σ_x characterize the amplitude of the noise for the surface temperature and wind stress curl, respectively. The detailed characteristics of the model are explained in Supplementary Discussion 3.

The parameters are set to $\beta = 0.5 - \alpha_0 b_0 \mu$, $\alpha = \alpha_0 + 0.005\mu$, $e = 0.00006 \times (b_0 \mu)^3$, $\gamma = 0.15 b_0 \mu$, $\varepsilon = 0.125$, $\alpha_0 = 0.075$, $b_0 = 8.6$, $\sigma_T = 0.25$ and $\sigma_x = 0.25$. For simplicity, the units of the parameters only have a time dimension in years. The coupling coefficient, μ , characterizes air–sea coupling strength and is directly linked with GMST as $\mu = 0.88 \times \text{GMST} - 13.59$. This linkage between μ and GMST considers increasing air–sea coupling strength by increasing open ocean area due to sea-ice loss in a warming climate. For the given parameter set, the Hopf bifurcation point of the model is $\text{GMST} = 16.5^\circ\text{C}$. The details of the parameter settings are explained in Supplementary Discussion 4.

To demonstrate the emergence of the oscillation by passing the Hopf bifurcation point, we increase the GMST from 14.8°C to 18.2°C for 6,000 years by applying $\text{GMST}(t) = 14.8^\circ\text{C} + (1.7/3,000)t$. The GMST passes the Hopf bifurcation point 16.5°C at year 3,000. The numerical integration of the model is performed using the stability-optimized adaptive scheme of strong order 1.5 for stochastic differential equations³⁸.

Data availability

The CMIP6 data are available from the Earth System Grid Federation repository (<https://esgf-node.llnl.gov/projects/cmip6/>). The LongRunMIP data are available upon request to Maria Rugenstein (maria.rugenstein@colostate.edu). The PlioMIP2 data are available upon request to Alan M. Haywood (a.m.haywood@leeds.ac.uk), and part of the data (CESM2, EC-Earth3-LR and GISS-E2-1-G) can be downloaded from the Earth System Grid Federation repository (<https://esgf-node.llnl.gov/projects/cmip6/>). The observational records are available as follows: HadCRUT5 (<https://www.metoffice.gov.uk/hadobs/hadcrut5/>); NOAA GlobalTemp5 (<https://www.ncdc.noaa.gov/products/land-based-station/noaa-global-temp> and <https://www.psl.noaa.gov/data/gridded/data.noaglobaltemp.html>); GISTEMP4 (<https://data.giss.nasa.gov/gistemp/>); and BerkeleyEarth (<https://berkeleyearth.org/data/>). The reanalysis data are available as follows: ERA5 (<https://www.ecmwf.int/en/forecasts/dataset/ecmwf-reanalysis-v5> and https://apdrc.soest.hawaii.edu/dods/public_data/Reanalysis_Data/ERA5) and NOAA-CIRES-DOE 20CRv3 (https://psl.noaa.gov/data/gridded/data.20thC_ReanV3.html).

Code availability

The code for the climate model data processing and analyses is available at <https://doi.org/10.6084/m9.figshare.27058846.v1> (ref. 59). The code for the conceptual model simulation is available at <https://doi.org/10.6084/m9.figshare.26889076.v2> (ref. 60).

References

50. Callahan, C. W. et al. Robust decrease in El Niño/Southern Oscillation amplitude under long-term warming. *Nat. Clim. Change* **11**, 752–757 (2021).
51. Babadi, B. & Brown, E. N. A review of multitaper spectral analysis. *IEEE Trans. Biomed. Eng.* **61**, 1555–1564 (2014).
52. Hasselmann, K. Stochastic climate models part I. Theory. *Tellus* **28**, 473–485 (1976).
53. Mann, M. E., Steinman, B. A., Brouillette, D. J. & Miller, S. K. Multidecadal climate oscillations during the past millennium driven by volcanic forcing. *Science* **371**, 1014–1019 (2021).
54. Mann, M. E. & Park, J. Oscillatory spatiotemporal signal detection in climate studies: a multiple-taper spectral domain approach. In *Advances in Geophysics* (eds Dmowska, R. et al.) Vol. 41, 1–131 (Elsevier, 1999).

55. Yang, J. The seasonal variability of the Arctic Ocean Ekman transport and its role in the mixed layer heat and salt fluxes. *J. Clim.* **19**, 5366–5387 (2006).
56. Danabasoglu, G. et al. The CCSM4 ocean component. *J. Clim.* **25**, 1361–1389 (2012).
57. O'Neill, L. W., Chelton, D. B. & Esbensen, S. K. The effects of SST-induced surface wind speed and direction gradients on midlatitude surface vorticity and divergence. *J. Clim.* **23**, 255–281 (2010).
58. Rackauckas, C. & Nie, Q. Stability-optimized high order methods and stiffness detection for pathwise stiff stochastic differential equations. In *Proc. 2020 IEEE High Performance Extreme Computing Conference (HPEC)* 1–8 (IEEE, 2020); <https://doi.org/10.1109/HPEC43674.2020.9286178>
59. Kim, S.-K. & An, S.-I. Code for the Arctic Ocean air-sea coupled mode analyses. *Figshare* <https://doi.org/10.6084/m9.figshare.27058846.v1> (2024).
60. Kim, S.-K. & An, S.-I. Numerical simulation code for the conceptual model of the Arctic Ocean air-sea coupled mode. *Figshare* <https://doi.org/10.6084/m9.figshare.26889076.v2> (2024).

Acknowledgements

S.-I.A. and S.-K.K. were supported directly by National Research Foundation of Korea (NRF-2018R1A5A1024958). S.-I.A. was supported directly by Yonsei Signature Research Cluster Program of 2024-22-0162, and by the Yonsei Fellowship, funded by Lee Youn Jae.

Author contributions

S.-K.K. conceived the idea and designed this study. S.-K.K. performed the analysis and produced the figures. S.-I.A. contributed to the analysis and interpretation of the results. S.-K.K. drafted the manuscript. S.-I.A. contributed to the writing of the manuscript.

Competing interests

The authors declare no competing interests.

Additional information

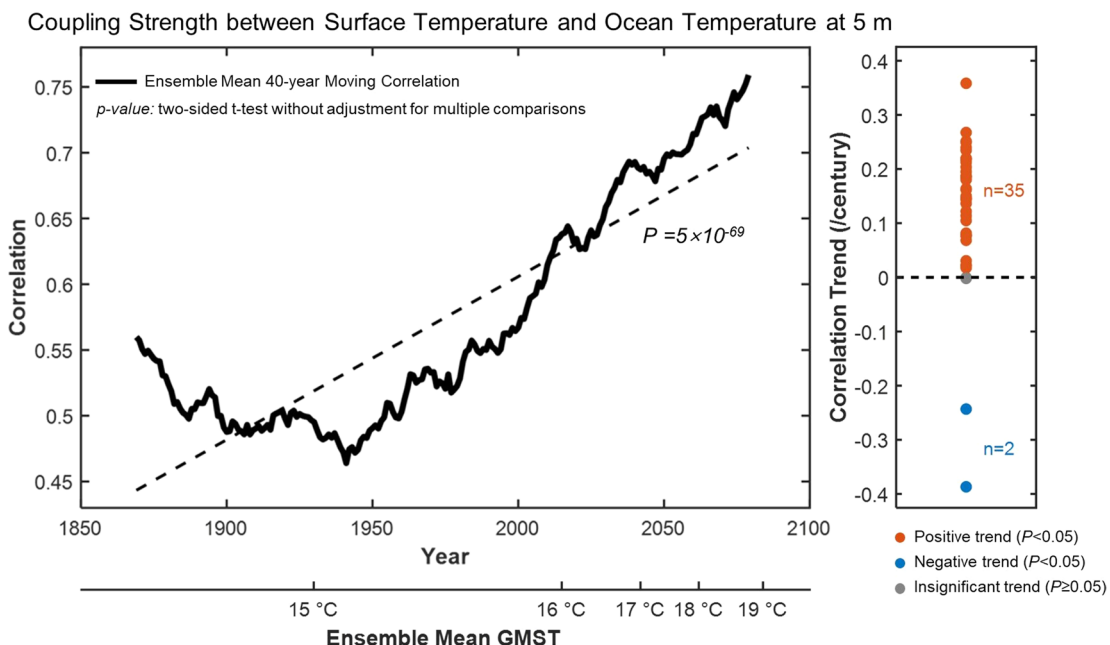
Extended data is available for this paper at <https://doi.org/10.1038/s41558-024-02171-3>.

Supplementary information The online version contains supplementary material available at <https://doi.org/10.1038/s41558-024-02171-3>.

Correspondence and requests for materials should be addressed to Soon-il An.

Peer review information *Nature Climate Change* thanks Dan Hodson and the other, anonymous, reviewer(s) for their contribution to the peer review of this work.

Reprints and permissions information is available at www.nature.com/reprints.

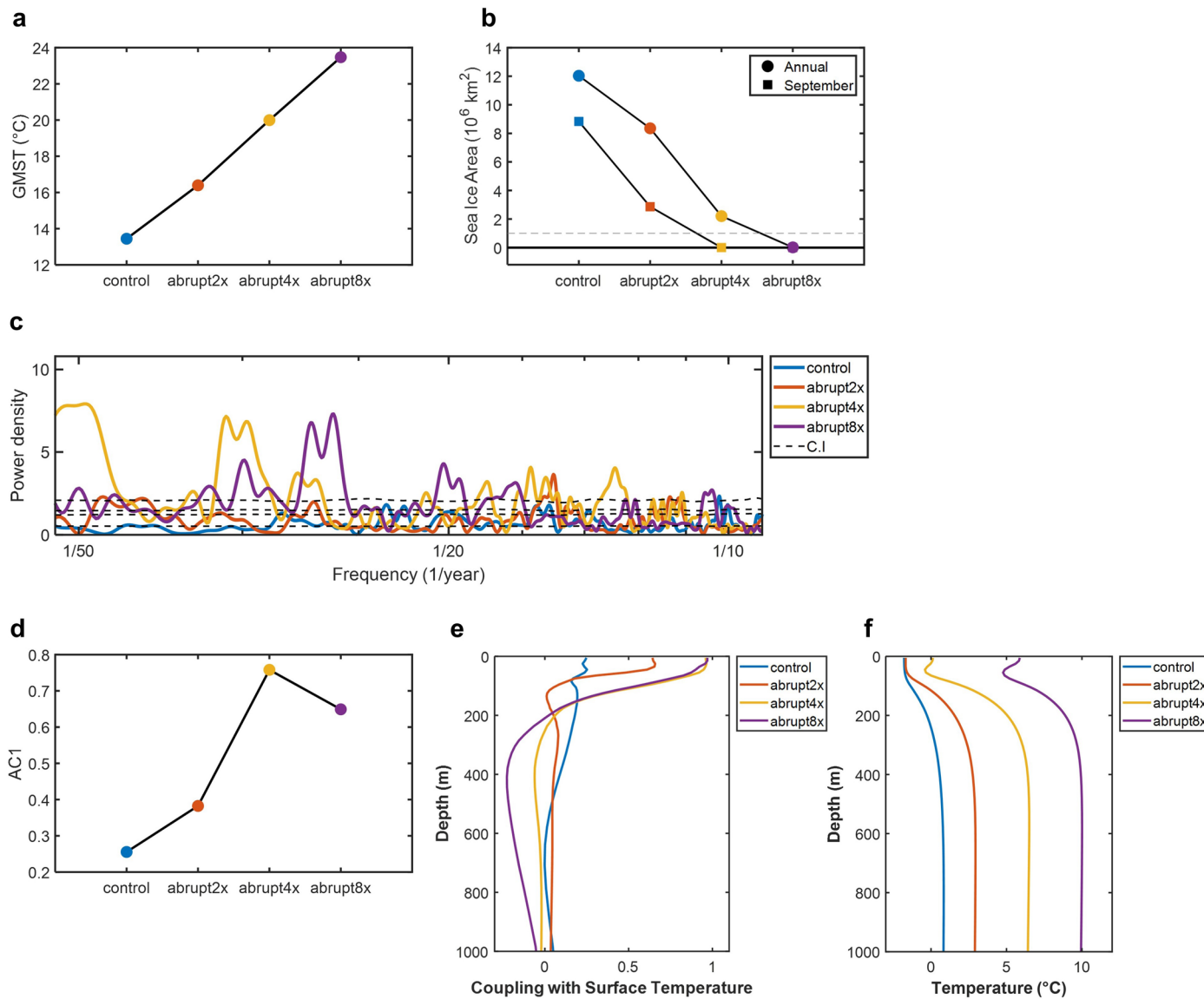

Extended Data Fig. 1 | Changes in air-sea coupling strength of the CMIP6 ensemble.

The multi-model ensemble mean 40-year moving correlation between the Arctic surface temperature and 5 m ocean temperature anomaly. The linear trend of correlation (dashed line). The lower horizontal axis displays the corresponding multi-model ensemble mean GMST to year (that is, black thick

line in Fig. 1a). The linear trend of 40-year moving correlation for each model (right panel). Models with a significant positive trend ($P < 0.05$) are marked with an orange dot, those with a significant negative trend ($P < 0.05$) are marked with a blue dot, and models with an insignificant trend ($P \geq 0.05$) are marked with a gray dot.

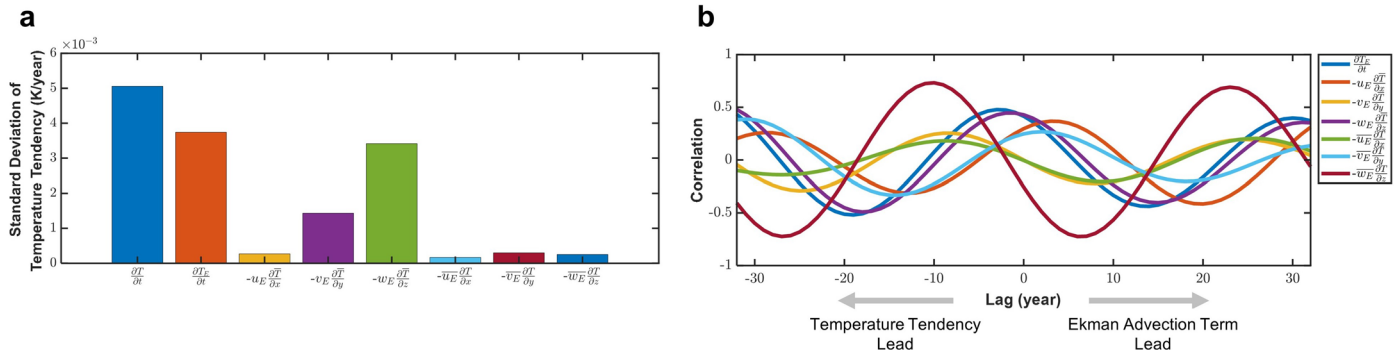


Extended Data Fig. 2 | The multitaper spectrum of the LongRunMIP ensemble. Each panel shows the results of each model. The multitaper spectrum (thick colored line) and the 50%, 90%, 95%, and 99% confidence level (dashed black line). In the legend, GMST is denoted.

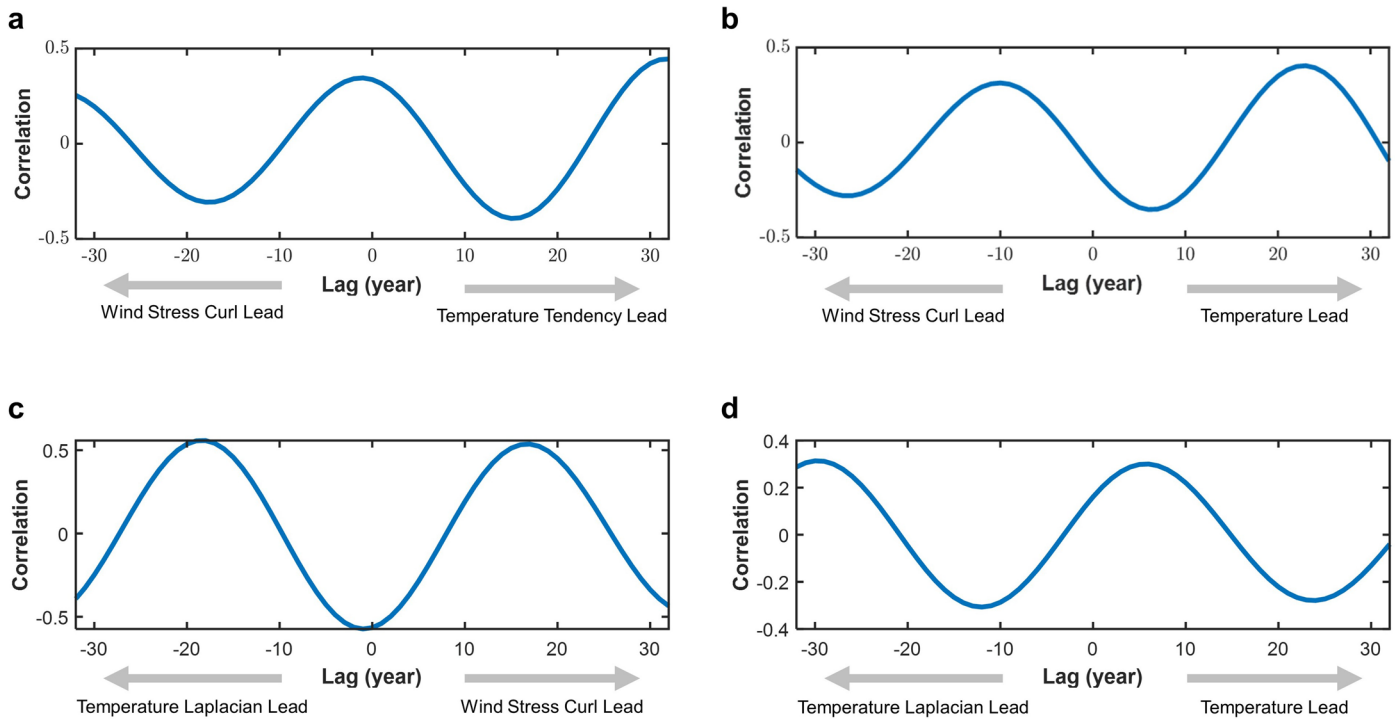


Extended Data Fig. 3 | Results of control, abrupt2x, abrupt4x, and abrupt8x experiments of the LongRunMIP CESM1.0.4. a. Global mean surface temperature (GMST). **b.** Arctic sea ice area in annual mean (circle) and September (square). **c.** Mutitaper spectrum of the Arctic surface temperature anomaly

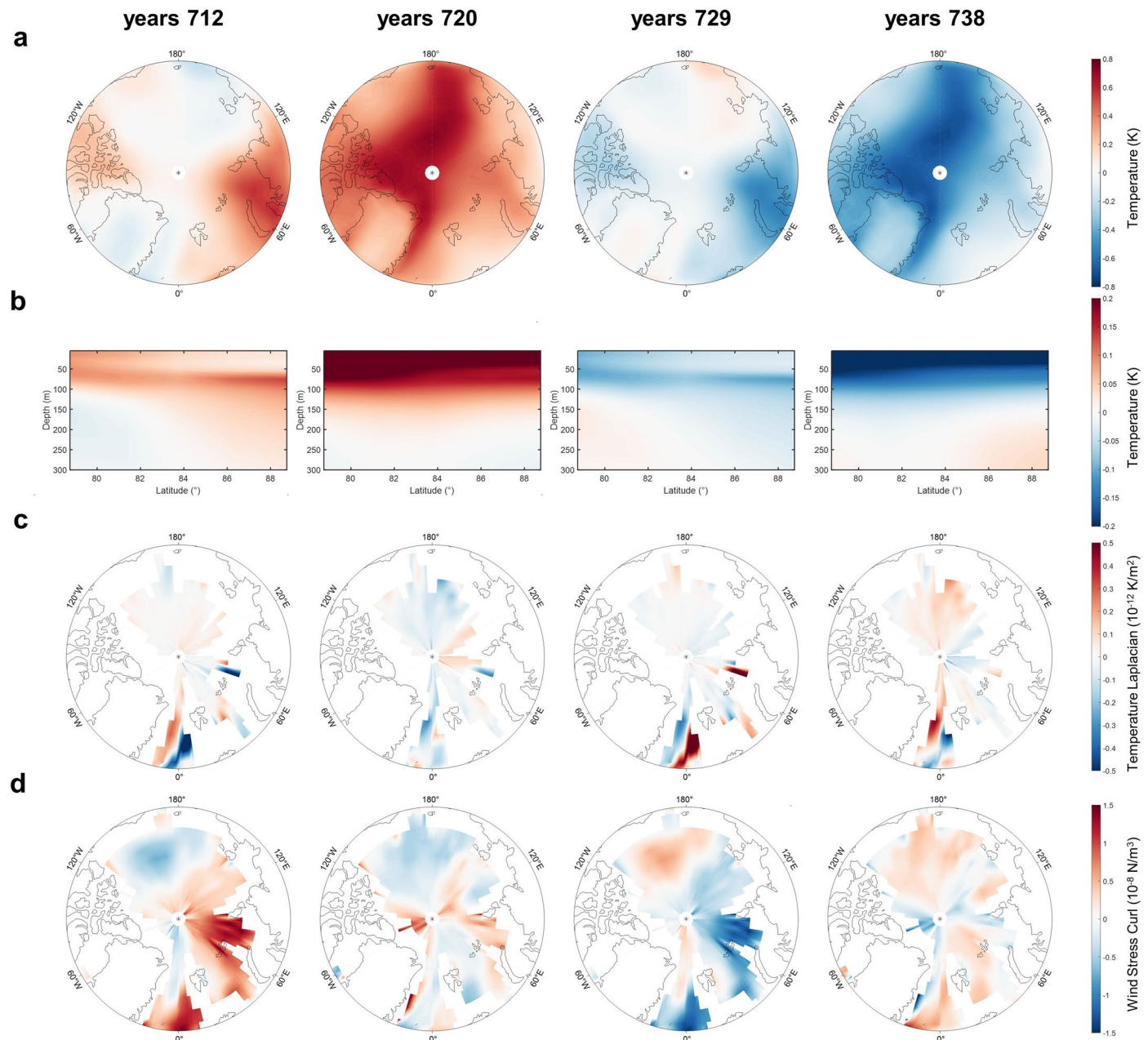
(same as the CESM104 panel in Extended Data Fig. 2). **d.** Lag-1 autocorrelation (AC1) of the Arctic surface temperature anomaly. **e.** Correlation between Arctic surface temperature and ocean temperature with depth. **f.** Arctic Ocean temperature profile.



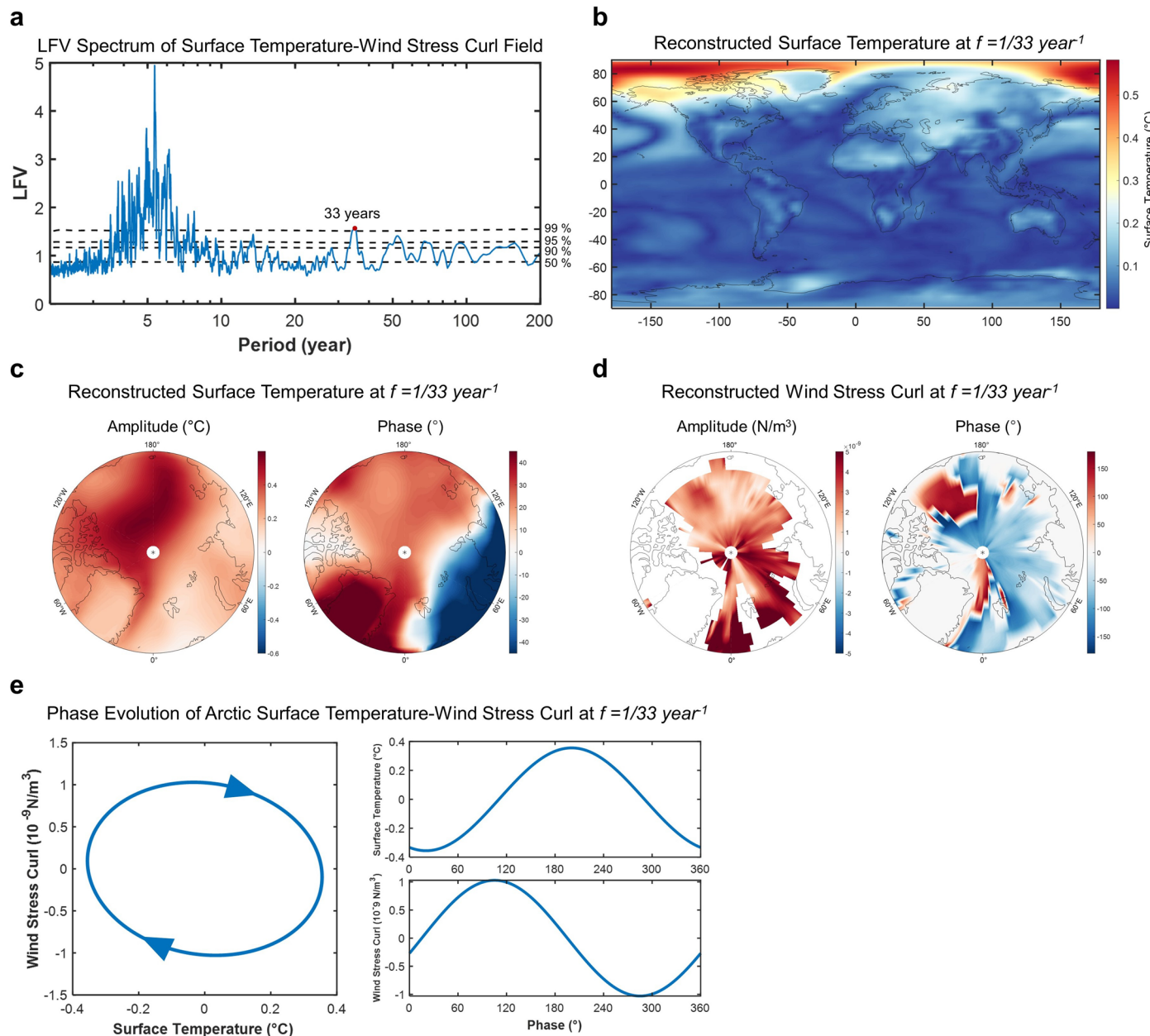
Extended Data Fig. 4 | The Ekman budget analysis for the CESM 1.0.4 abrupt4x experiment. **a.** The standard deviation of the ocean temperature tendency and Ekman advection terms. **b.** The lead-lag correlation between the ocean temperature tendency and Ekman advection terms.



Extended Data Fig. 5 | The lead-lag correlation analysis of the CESM 1.0.4 abrupt4x experiment. **a.** wind stress curl and surface temperature tendency. **b.** wind stress curl and surface temperature. **c.** surface temperature Laplacian and wind stress curl. **d.** surface temperature Laplacian and surface temperature.

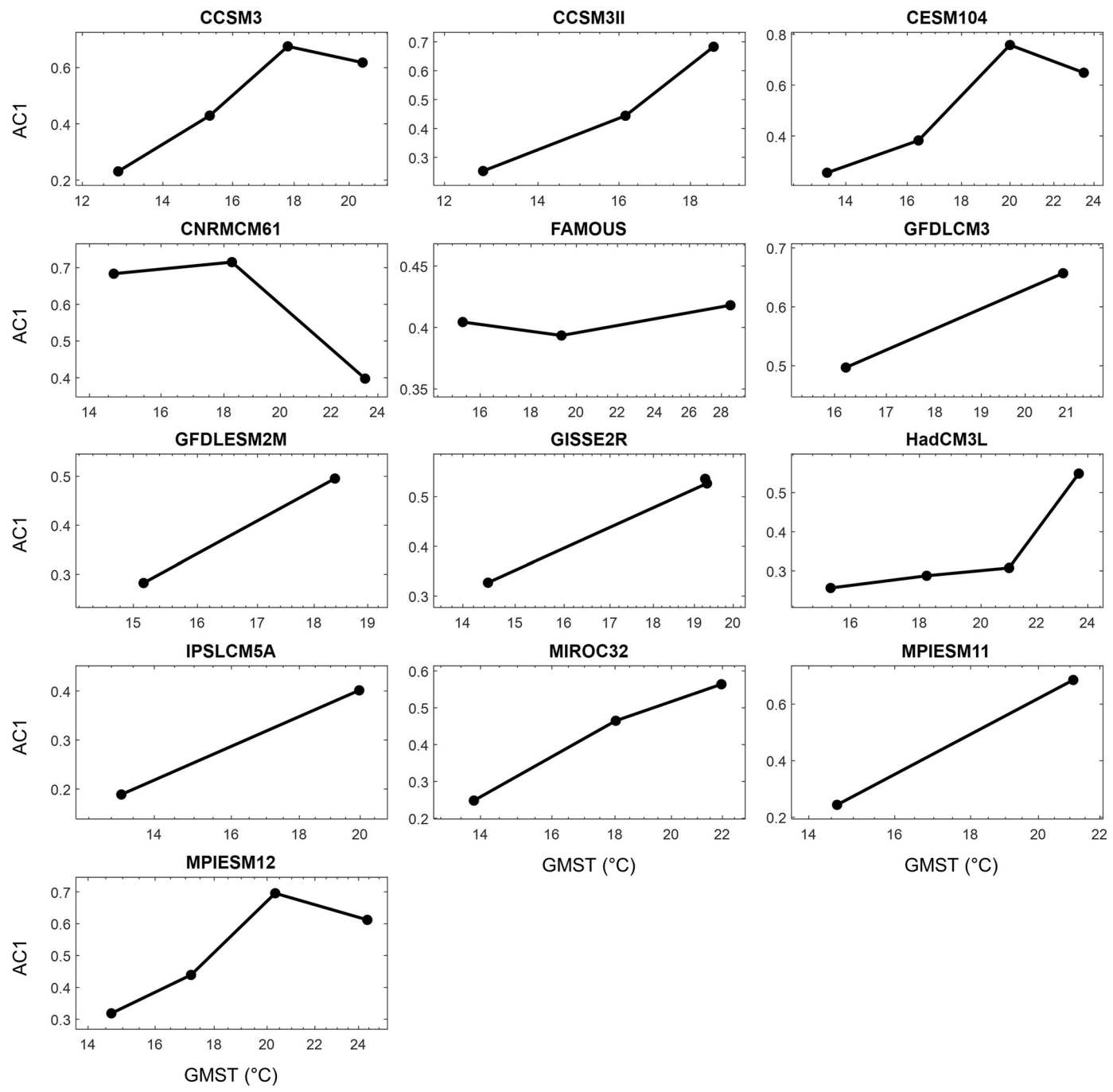


Extended Data Fig. 6 | Evolution of Arctic surface temperature and wind stress curl anomalies during years 712 to 738 in the CESM1.0.4 abrupt4x experiment.
a. Surface temperature. **b.** zonal mean ocean temperature by depth. **c.** sea surface temperature Laplacian. **d.** wind stress curl.

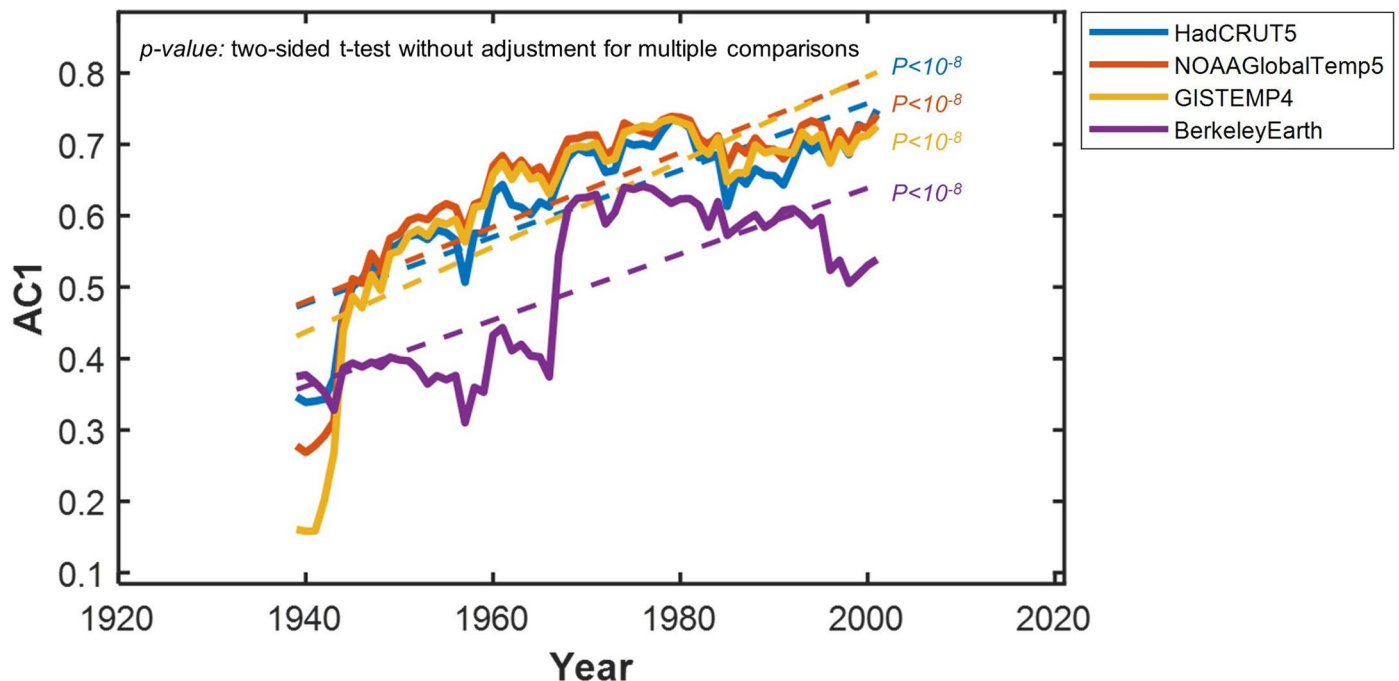


Extended Data Fig. 7 | The MTM–SVD analysis of the CESM1.0.4 abrupt4x experiment. The MTM–SVD analysis is performed for joint global surface temperature and wind stress curl anomaly field of the CESM1.0.4 abrupt4x experiment. **a.** LFV spectrum. The 50%, 90%, 95%, and 99% confidence levels against the red noise null hypothesis are marked as black dashed lines. The spectral peak at the period of 33 years is marked as a red dot. **b-e.** The reconstructed surface temperature and wind stress curl anomaly at the period

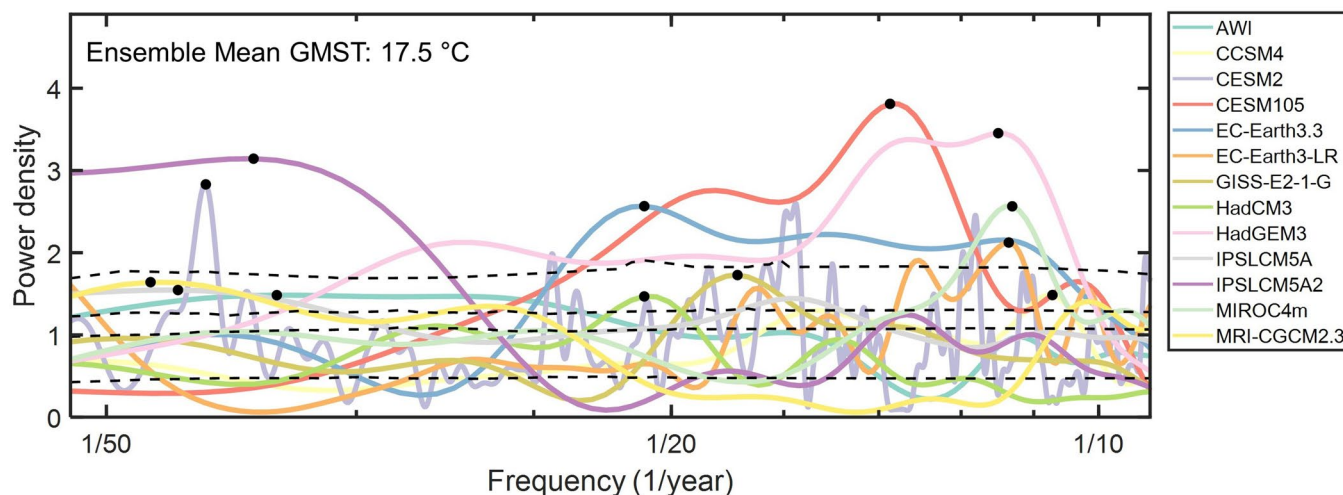
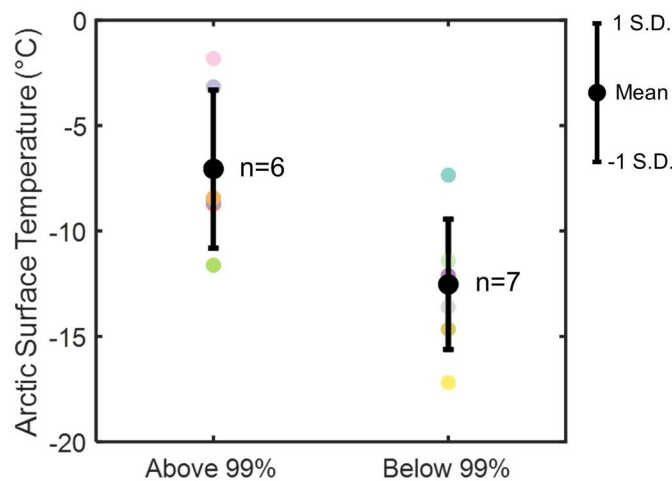
of 33 years. **b.** The amplitude of the reconstructed surface temperature anomaly. **c.** The amplitude and phase of the reconstructed surface temperature anomaly over the Arctic. **d.** Same as **c**, but for the wind stress curl anomaly. **e.** The reconstructed surface temperature and wind stress curl anomaly are averaged over the Arctic (80°N - 90°N). The right panels show the phase evolution of the surface temperature and wind stress curl anomaly, and their trajectory is shown in the left panel.



Extended Data Fig. 8 | AC1 of the LongRunMIP ensemble. Each panel shows the AC_1 of the Arctic surface temperature anomaly for each model. AC_1 is plotted against GMST. All models except CNRMCM61 and FAMOUS show an increasing trend in AC_1 against GMST. The time series of surface temperature anomaly is shown in Supplementary Fig. 6.



Extended Data Fig. 9 | AC1 of the Arctic surface temperature anomaly from four in-situ observational records during 1920–2021. The thick colored line is the 40-year moving AC1. The dashed line is a linear regression line. A p-value of the linear regression is also shown.

a**b**

Extended Data Fig. 10 | The multitaper spectrum of the Arctic surface temperature anomaly of the PlioMIP2 ensembles. **a.** Thick colored lines are the power spectrum for each PlioMIP2 model. The 50%, 90%, 95%, and 99% confidence levels against the red noise null hypothesis are marked as black

dashed lines. The local spectral peak is marked as a black dot. **b.** Arctic surface temperature climatology in two different groups of models in which the spectral peak is above and below the 99% confidence level. The mean and one standard deviation are shown as a large black circle and error bar.